Predicting Microstructure Properties Using Transfer Learning

Farzana Tasnim[*]; Joshua Grose[*]; Nathan F Sheu[*]; Remi Dingreville[†]; Michael Cullinan[*];
[*]University of Texas at Austin; [†]Sandia National Laboratories

Abstract

This study explores the application of transfer learning using pre-trained convolutional neural networks (CNNs) to investigate the relationship between process parameters and microstructure evolution in scientific applications, aiming to predict their correlation with the process conditions between laser-sintered samples and fully sintered samples. This method is demonstrated using a dataset composed microstructure images taken from samples fabricated via micro-Selective Laser Sintering (μ-SLS). The proposed approach utilizes pre-trained CNNs to extract informative features from Scanning Electron Microscope (SEM) images and train a fully connected neural network to predict the process parameter, i.e. the exposure time of a given sample microstructure. The model achieves high accuracy in predicting the process condition directly from SEM images, even when dealing with noisy and varied datasets. An accuracy of 94% and 86% was achieved when performing binary classification of lightly sintered and heavily sintered images. When extended to multiclass classification with 5 unique degrees of sintering, an accuracy of 78% was achieved. This approach offers computational efficiency via transfer learning, robust noise handling, and the ability to generalize to unseen data. This modeling framework has the potential for extension into scientific fields needing microstructure analysis and process-property understanding beyond μ-SLS.

Keywords

Micro-Selective Laser Sintering (μSLS), Transfer learning, Scanning Electron Microscope (SEM) images, Process parameter prediction, Microstructure analysis

Introduction

The increasing demands on computational resources necessitate a reduction in transistor sizes to pack more transistors into the same chip area [1], which limits the applicability of existing technologies in critical fields such as advanced semiconductor packaging [2]. The Microscale Selective Laser Sintering (μ-SLS) system, developed at the University of Texas at Austin [3], addresses this challenge by enabling the production of copper and silver structures with single-micrometer feature resolutions [4]. As microscale additive manufacturing gains importance across various sectors, including electronics, biotechnology, medical devices, and optics, driven by the growing demand for miniaturization, μ-SLS emerges as a leading technique to meet these challenges. This method utilizes laser energy to selectively sinter nanoparticles, making it particularly adept at fabricating complex 3D interconnect structures [5]. μ-SLS is positioned as a key technology in microelectronics packaging due to its ability to precisely deposit material layers [6] and construct final components through selective laser sintering. The μ-SLS process integrates sophisticated optics and motion systems to achieve exceptional resolution and throughput, with spot sizes as small as 1 μm and single-micrometer resolution [7][8]. Variations in process parameters during μ-SLS result in diverse microstructures, each with unique topological features.

Understanding the correlations between process conditions, microstructures, and resultant properties is crucial for producing high-quality thin films in μ-SLS. This study aims to identify and elucidate these intricate pattern-forming processes, known as topological transitions, in thin films produced by μ-SLS. By analyzing SEM images under varying process conditions, including both images with known parameters (such as power and exposure time), we developed a classification model to recognize differences between these images and predict process parameters for new SEM images, despite the challenges in visual differentiation.

Recent advances in machine learning and deep learning have substantially improved SEM image analysis capabilities. For example, Modarres et al. [9] applied transfer learning to classify 20,000 SEM images into 10 categories, such as particles, nanowires, and films, using image recognition and automatic labeling. Ziatdinov et al. [10] developed a deep neural network workflow to extract atomic positions, defect structures, and track defect transformations from unprocessed STEM data, identifying atomic locations and defects within a lattice. Madsen et al. [11] developed a deep learning algorithm using a convolutional neural network to identify local structures in atomic-resolution TEM images, effectively classifying atomic structures and distinguishing chemical types and column heights while remaining robust to varying microscope parameters and noise. De Haan et al. [12] used deep learning to enhance low-resolution SEM images by inferring unresolved features, which were validated against high-resolution images of the same sample. Pellegrino et al. [13] developed a machine learning model to predict the morphology of TiO2 nanoparticles based on synthesis parameters like size, polydispersity, and aspect ratio. They also reverse-engineered the process to create nanoparticles with ideal morphology. Lee et al. [14] used a genetic algorithm to optimize the analysis of TEM images, efficiently clustering nanoparticles based on five morphological parameters—major and minor axis length, area, solidity, and angular distance—into groups with similar properties. Monchot et al. [15] developed a deep learning-based segmentation algorithm using Mask-RCNN and transfer learning to define the boundaries of titanium dioxide particles in SEM images, improving generalization in agglomerate analysis. Shen et al.[16] developed a Faster R-CNN system for analyzing scanning transmission electron microscope images, effectively detecting and analyzing defects like dislocation loops in irradiated ferritic steels by identifying various morphologies and extracting geometrical information through a two-stage detector with a region proposal network and an ROI regressor. Lee et al. [17] developed a dual deep learning network for robust autofocusing in SEM. The autofocusing-evaluation network (AENet) evaluated image quality on a scale from 0 to 9, using both SEM images and magnification data, while the autofocusing-control network (ACNET) controlled the SEM in real time based on AENet's outputs. Dahy et al. [18] developed a neural network to classify Pd nanoparticles in SEM images, using an optimization model to identify features like lines, intersections, and shapes.

Building on these impressive advancements, this research is distinguished by the specific targeting of the detection and monitoring of sintering in μ-SLS thin films. This novel approach allows for the precise identification and control of process conditions, thereby optimizing material properties and mitigating defects. Using advanced classification models in conjunction with SEM image analysis, a refined tool for enhancing the μ-SLS manufacturing process is provided. This advancement results in improved process control and facilitates the production of high-quality, nanostructured materials, thus advancing the field of additive manufacturing and supporting the development of tailored, defect-free products high quality sintered parts.

Experimental Method

The experimental procedure began with the preparation of a glass slide, onto which CI-005 copper nanoparticle ink from NovaCentrix was applied. (Figure 1-a) The ink was spin-coated at 750 rpm with an acceleration of 30 m/s² for 30 seconds to ensure a uniform film, then dried on a hot plate at 80°C. (Figure 1-b & c) The micro-Selective Laser Sintering (μ-SLS) process was performed with an operating current of 55A and a voltage of 20V. (Figure 1-e)

a) 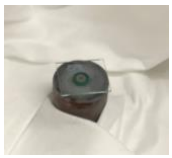 b)  c)  d)  e) 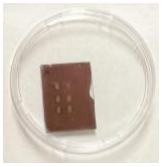

Figure 1: Experimental procedure a) clear glass slide on a spin coater b) spin-coated copper ink on the glass slide c) wet ink on a hot plate for drying d) dried ink e) laser sintered particle

Key parameters in this process include Burst Count and Duty Cycle. Burst Count represents the number of laser pulses applied to a specific area and serves as an indicator of exposure time—e.g., a Burst Count (BC) of 100 corresponds to an exposure duration of 1 second. Higher burst counts lead to extended exposure and increased energy input, which facilitates greater necking between particles. Figure 2 shows the evolution of sintering through the formation of necking. This enhanced necking improves particle bonding, reduces porosity, and increases the material's density and mechanical strength. This phenomenon has been explained elaborately in our previous work [19]. A higher duty cycle increases laser activity, enhancing energy input, nanoparticle diffusion, and necking for improved material densification. As it nears 100%, the process resembles continuous wave laser sintering, providing constant heating and further the material.

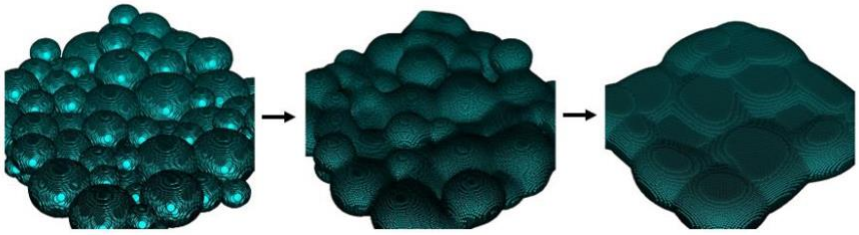

Figure 2: Evolution of sintering [20]

Workflow of the Model

The sintered parts were examined using SEM to capture images. For consistency, images were taken at the center of each sample. The microstructure of each part was analyzed to observe the visibility of the nanoparticles (Figure 3a). A data descriptor file is created to document all parameters used during image processing (Figure 3b), with a specific focus on Burst Count, given that power remains constant. The borders of the SEM images are then cropped to concentrate on the microstructure (Figure 3c). The intensity distribution within each image is adjusted using the histogram equalization to enhance visibility and highlight key features (Figure 3d).

To match the input size required by standard, pre-trained CNN models, large SEM images are randomly sampled to produce a set of smaller images. 40 smaller patches are sampled from each base SEM image to produce an augmented dataset. Transformations such as Random Crop, Random Horizontal Flip, and Random Rotation are applied to introduce diversity, allowing the generation of unique patches, with overlapping crops permitted if necessary (Figure 3e). The patches are then simplified by undergoing Grayscale Conversion, Convert to Tensor, and Normalization processes. These processed patches are saved as pickle files to facilitate efficient handling. Additionally, a data descriptor file is created for the patched images, which is used for subsequent analysis and processing (Figure 3f).

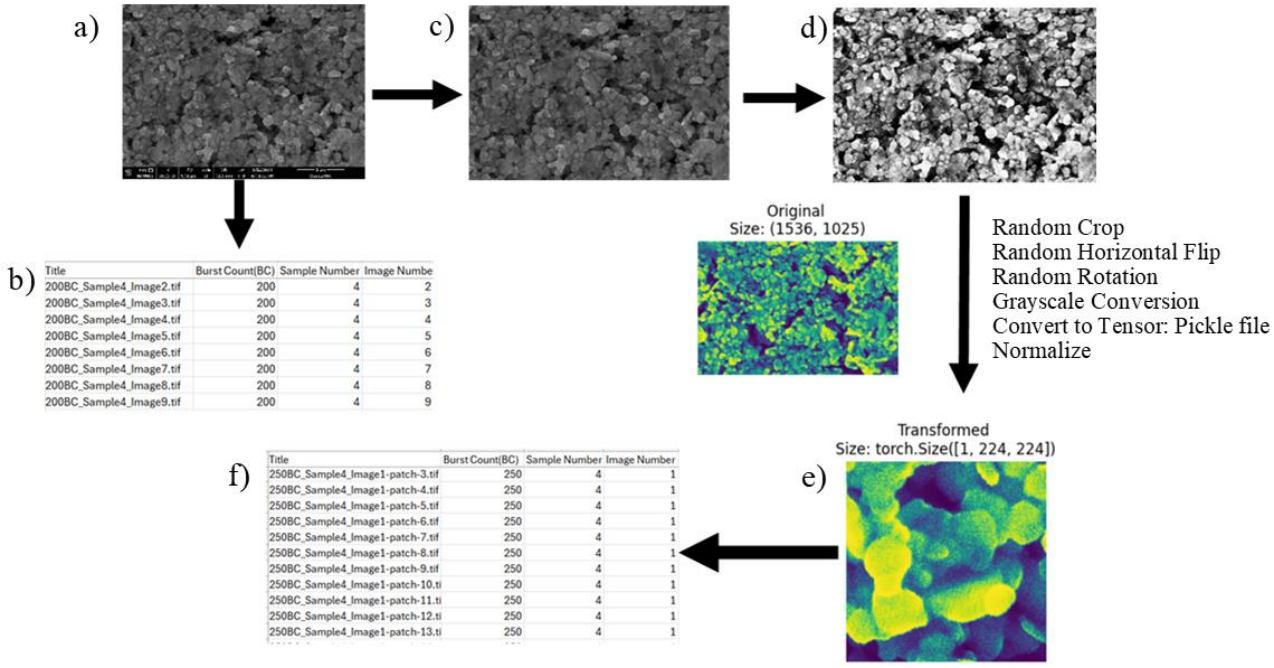

Title	Burst Count(BC)	Sample Number	Image Numbe
200BC_Sample4_Image2.tif	200	4	2
200BC_Sample4_Image3.tif	200	4	3
200BC_Sample4_Image4.tif	200	4	4
200BC_Sample4_Image5.tif	200	4	5
200BC_Sample4_Image6.tif	200	4	6
200BC_Sample4_Image7.tif	200	4	7
200BC_Sample4_Image8.tif	200	4	8
200BC_Sample4_Image9.tif	200	4	9

Title	Burst Count(BC)	Sample Number	Image Number
250BC_Sample4_Image1-patch-3.tif	250	4	1
250BC_Sample4_Image1-patch-4.tif	250	4	1
250BC_Sample4_Image1-patch-5.tif	250	4	1
250BC_Sample4_Image1-patch-6.tif	250	4	1
250BC_Sample4_Image1-patch-7.tif	250	4	1
250BC_Sample4_Image1-patch-8.tif	250	4	1
250BC_Sample4_Image1-patch-9.tif	250	4	1
250BC_Sample4_Image1-patch-10.ti	250	4	1
250BC_Sample4_Image1-patch-11.ti	250	4	1
250BC_Sample4_Image1-patch-12.ti	250	4	1
250BC_Sample4_Image1-patch-13.ti	250	4	1

Figure 3: Image Preprocessing a) The original SEM image, b) Data Descriptor file with the original images, c) SEM image without border, d) Adjusted SEM image after the intensity distribution, e) Creating patches from the adjusted images, f) Creating data descriptor file for the patches

Despite cropping, the patches retain large pixel dimensions. To address this, the patches are processed through a pretrained ConvNext network, which effectively captures relevant features from the SEM images. A pretrained ConvNext network is well-suited for scenarios with limited data. The model is first loaded onto a CPU or GPU to accelerate processing. ConvNext is adapted for feature extraction by removing the classification layer, and the model is set to evaluation mode to freeze the image processing layers, disabling dropout and ensuring consistent outputs during feature extraction. Next, the image patches are loaded from the pickle file and transferred to the same device as the model (Figure 4a). ConvNext is then used to extract features from these patches, which are compiled into a single tensor for subsequent analysis (Figure 4b). The resulting low-dimensional representations are input into a classification model trained to predict the process parameters.

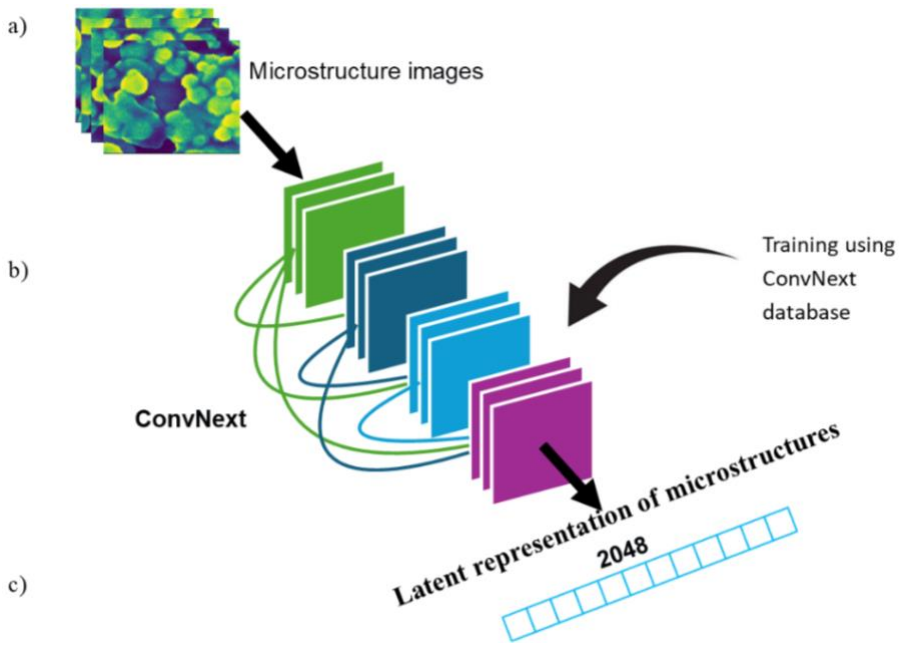

Figure 4: Extracting feature using ConvNext a) Patches from the tensor file, b) Training using ConnvNext, c) Compile the extracted features to tensor

To predict process parameters from SEM images, a neural network with three hidden layers, each employing ReLU activation functions, is utilized. Dropout and Weight Decay are applied to prevent overfitting, while Batch Normalization is used to stabilize and accelerate training. The features extracted from SEM image patches and the associated process parameters are provided as input to the network. The dataset is divided into 80% for training, 10% for testing, and 10% for validation. The model is trained with a learning rate of 0.001, and seeds are set to ensure reproducibility. A batch size of 32 is used, allowing 32 data points to be processed per iteration, and the model is trained for 1000 epochs, with validation performed every 10 epochs. A graph of training and validation losses over the epochs is plotted to track learning progress and guide model adjustments.

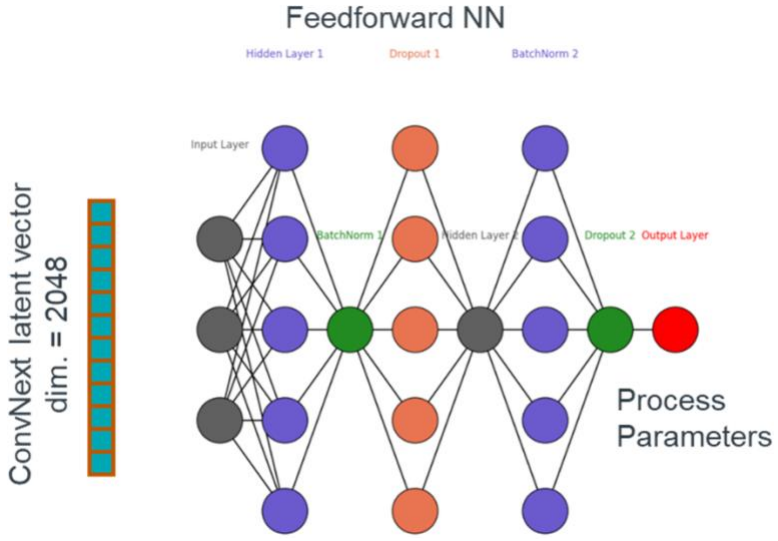

Figure 5: Neural Network to Solve the Inverse Problem

Results and Discussion

Principal Component Analysis (PCA) was initially tested as a simpler method for classifying the data. Although PCA is useful for retaining key information and recognizing patterns, clear clusters corresponding to specific process parameters were not observed. Due to the limitations of PCA in providing distinct classifications, a more advanced approach using neural networks was adopted, resulting in better performance for this task.

The classification model was applied to a binary classification task to evaluate its performance. A total of twelve samples, six each from 100BC as class 0 and 250BC as class 1(Figure 6a- i & ii), were used, with 10 images captured per sample and 40 patches generated per image, yielding a dataset of 4,800 patches. The data was divided into 80% for training and 20% for testing, resulting in 480 patches in the test set. The training and validation loss graph shows that the training loss decreases sharply and stabilizes near zero, indicating strong model learning on the training data (Figure 6b).

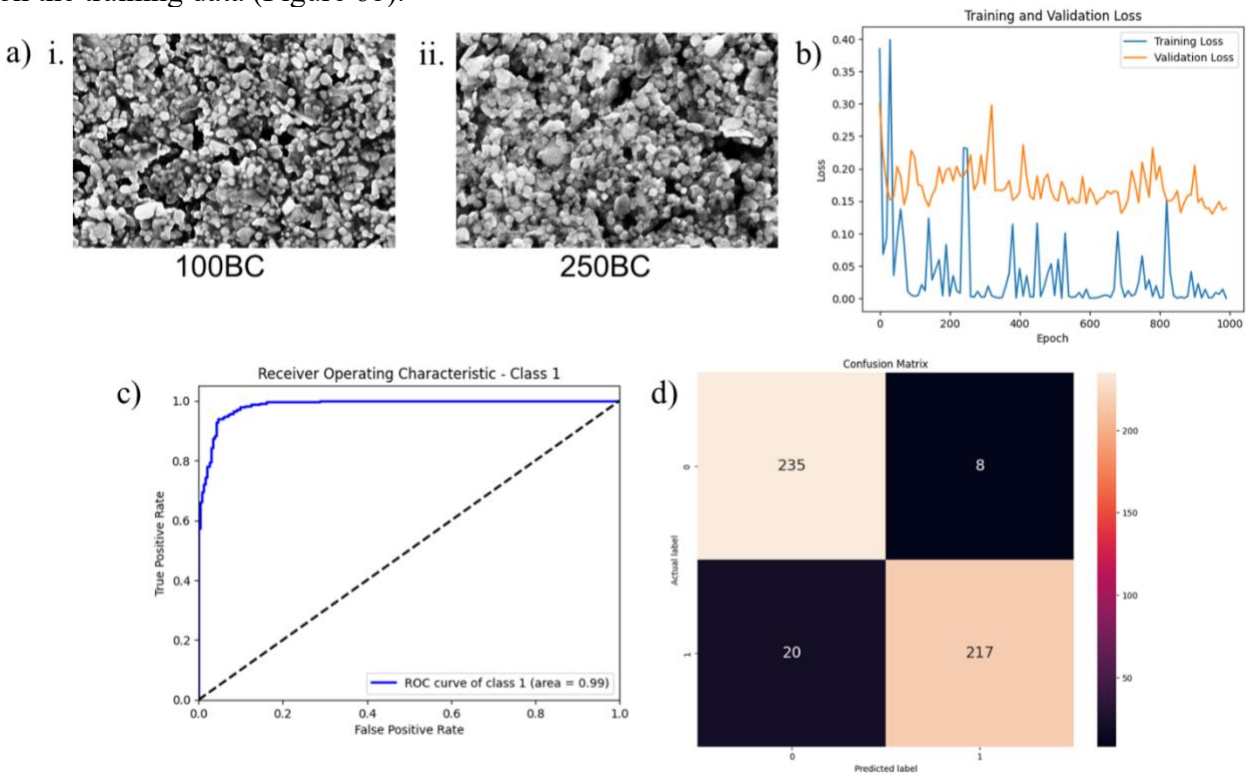

Figure 6: For 100BC and 250BC: a) SEM image i) 100BC and ii) 250BC, b) Training and validation loss graph c) ROC curve d) Confusion Matrix

The Receiver Operating Characteristic (ROC) curve shows that the model exhibits excellent classification performance for class 1 (AUC = 0.99) (Figure 6c). This indicates that the model effectively identifies class 1. The confusion matrix reveals that the model correctly predicted 235 true negatives (class 0) and 217 true positives (class 1), with 8 false positives and 20 false negatives, reflecting relatively balanced performance with a few misclassifications in both classes (Figure 6d). The F1-Score for the classification model was 0.94, indicating strong overall performance in terms of precision and recall, largely due to the distinct microstructural differences between the 100BC and 250BC Burst Counts.

A separate model was assessed for its ability to differentiate between samples with closer Burst Counts, specifically using six samples each of 150BC and 200BC (Figure 6a- i & ii). The dataset, including SEM images and patches, was consistent with previous experiments. The training and validation loss graphs, plotted over 1000 epochs, show that while the training loss decreases significantly, the validation loss fluctuates and remains relatively high, suggesting possible overfitting. (Figure 7b).

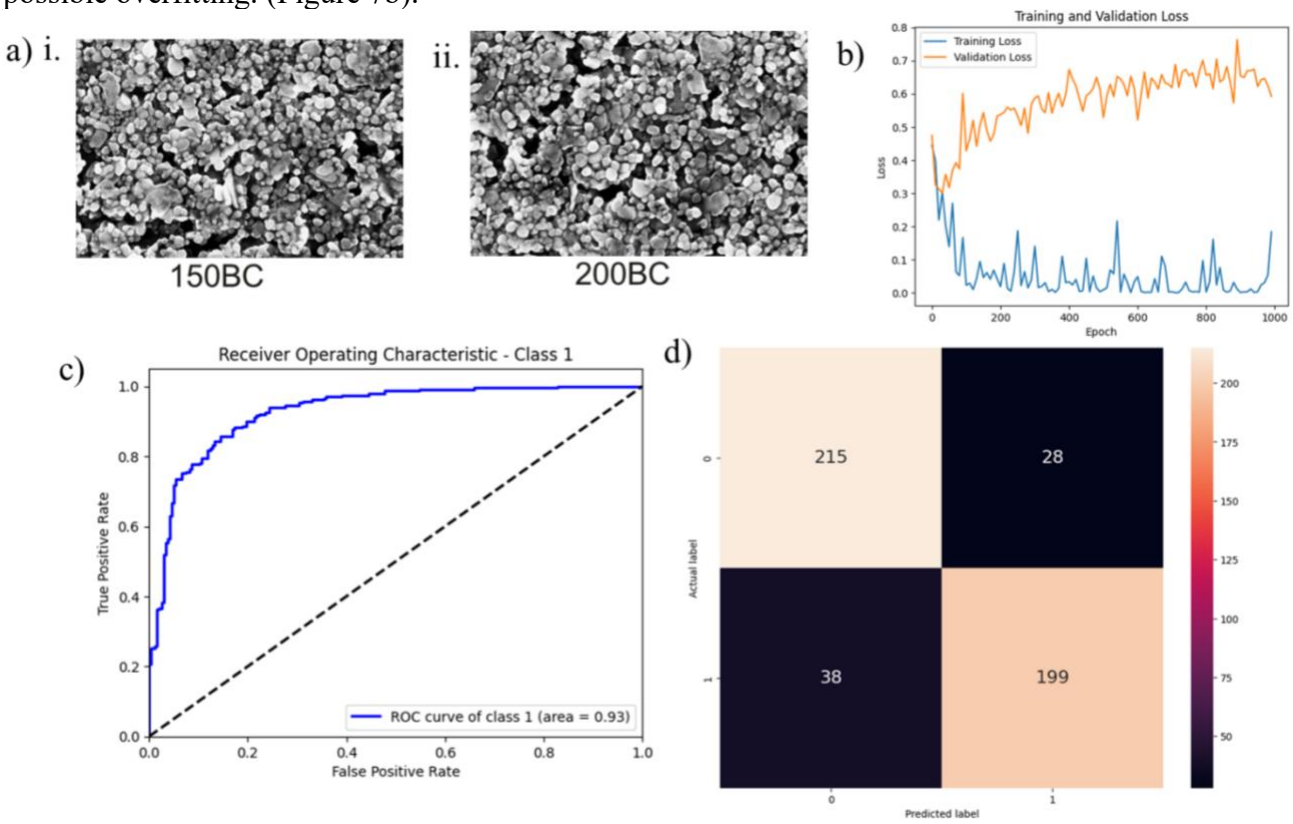

Figure 7: For 150BC and 200BC a) SEM image i) 150BC and ii) 200BC, b) Training and validation loss graph, c) Confusion Matrix

The ROC curve for this multi-class classification problem indicates a high AUC of 0.93 for class 1, signaling good performance. (Figure 7c). The confusion matrix reveals that the model accurately predicted 215 true negatives (class 0) and 199 true positives (class 1), with 28 false positives and 38 false negatives (Figure 7d). The model's F1-Score was 0.86. While this accuracy is slightly lower compared to previous tests, it still demonstrates commendable performance given the challenge of distinguishing between microstructures with closely related Burst Counts. This highlights the model's robustness in handling nuanced variations in microstructural transitions.

The model demonstrated strong performance in binary classification tasks. To further evaluate its capabilities, we conducted a multiclass classification assessment using six sample sets with Burst Counts ranging from 50BC to 250BC (Figure 8a i-v). The samples were sintered across three different slides, each containing two sets. A total of 300 images were analyzed, which were segmented into 120,000 patches for detailed examination. This multiclass evaluation aimed to test the model's robustness in distinguishing between various microstructural variations. Class 0

corresponds to 50BC, Class 1 to 100BC, Class 2 to 150BC, Class 3 to 200BC, and Class 4 to 250BC. Analysis of the training and validation loss over 1000 epochs revealed steady decreases in training loss, indicating effective learning (Figure 8b). However, the validation loss plateaued after a certain point, suggesting potential overfitting.

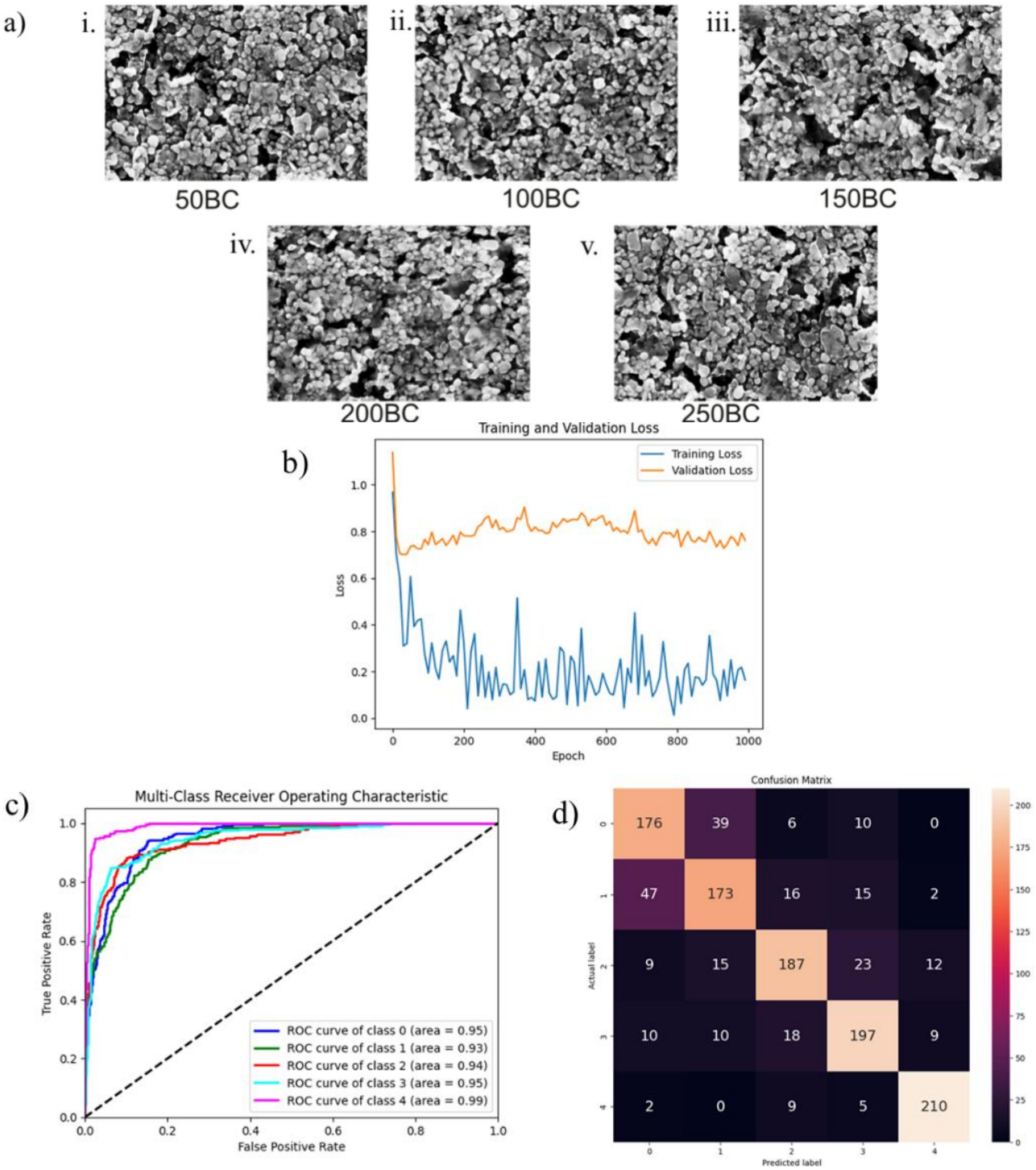

Figure 8: a) SEM images: i.50BC, ii. 100BC, iii. 150BC, iv. 200BC, v. 250BC, b) Training and validation loss graph, c) Multi-Class Receiver Operating Characteristic, d) Confusion Matrix

ROC curve analysis demonstrated strong performance across different classes, with AUC values ranging from 0.93 to 0.99 (Figure 8c). These high AUC values indicate the model's effectiveness in differentiating between classes, with ROC curves positioned well above the diagonal line representing random guessing. Class 4 (250BC) showed the best performance, while Class 1 (100BC) exhibited slightly lower performance compared to the other classes. The ROC curves provide a comprehensive view of the model's classification quality, where higher AUC values correspond to better performance.

The confusion matrix offers additional insights into the model's classification accuracy (Figure 8d). Class 0 (50BC) achieved a strong true positive rate with 176 correct classifications, although some misclassifications occurred into Class 1 (100BC), Class 2 (150BC), and Class 3 (200BC). Class 1 (100BC) had 173 correct classifications but showed notable misclassifications into Class 0 (50BC), Class 2 (150BC), Class 3 (200BC), and Class 4 (250BC). Class 2 (150BC) and Class 3 (200BC) also exhibited high true positive rates, though some instances were misclassified into other classes. Class 4 (250BC) had the highest true positive rate with 210 correct classifications and minimal misclassifications. While the model performed well overall, distinguishing between classes with similar Burst Counts remains a challenge.

Challenges and Future Work

Future work could involve expanding the network to include a wider range of process conditions, such as varying power levels, using SEM images. Integrating a regression model could enhance prediction precision by offering more nuanced output estimates. Key challenges to address include ensuring accurate data collection with minimal gaps in burst counts and integrating SEM images with supplementary data types, such as resistivity measurements, to further refine model accuracy. The ultimate goal is to predict the optimal parameters needed to achieve a desired microstructure, with a particular focus on conductivity.

Conclusion

In conclusion, this study demonstrates the effectiveness of leveraging SEM images and advanced machine learning techniques for classifying and predicting process parameters in micro-Selective Laser Sintering (μ-SLS). The model exhibited high accuracy, excelling particularly in binary classifications and showing promising performance in multiclass scenarios. The integration of dimensionality reduction and feature extraction using ConvNext, alongside a well-constructed neural network, provides a robust framework for analyzing and predicting process conditions based on microstructural features. Future work will focus on expanding the model's scope to encompass a broader range of process conditions, incorporating additional data types for improved accuracy, and refining data collection methodologies to better handle burst count variations. Ultimately, this research aims to achieve precise control over process parameters, thereby optimizing microstructural properties and advancing the fields of materials science and additive manufacturing.

Acknowledgment

This research was supported by the National Science Foundation under grant number 2141044. We extend our gratitude to the NSF for their invaluable support in making this study possible.

References

[1] A. Allan, D. Edenfeld, W. H. Joyner, A. B. Kahng, M. Rodgers, and Y. Zorian, "2001 technology roadmap for semiconductors," *Computer*, vol. 35, no. 1, pp. 42–53, Jan. 2002, doi: 10.1109/2.976918.

[2] J. U. Knickerbocker *et al.*, "3D silicon integration," in *2008 58th Electronic Components and Technology Conference*, May 2008, pp. 538–543. doi: 10.1109/ECTC.2008.4550025.

[3] "Methods of Additive Manufacturing | School of Architecture." Available: https://soa.utexas.edu/events/methods-additive-manufacturing

[4] N. Roy, A. Yuksel, and M. Cullinan, "Design and Modeling of a Microscale Selective Laser Sintering System," doi: 10.1115/MSEC2016-8569.

[5] A. Liao, J. Grose, F. Tasnim, and M. Cullinan, "Additive manufacturing of metal interconnects using microscale selective laser sintering," in *Nanoscale and Quantum Materials: From Synthesis and Laser Processing to Applications 2023*, SPIE, Mar. 2023, pp. 19–20. doi: 10.1117/12.2655264.

[6] "PART SCALE SIMULATION OF HEAT AFFECTED ZONES FOR PARAMETER OPTIMIZATION IN A MICROSCALE SELECTIVE LASER SINTERING SYSTEM." Available: https://repositories.lib.utexas.edu/items/104069a0-8218-47ef-9589-31f773bc4c5f

[7] N. K. Roy, C. S. Foong, and M. A. Cullinan, "Effect of size, morphology, and synthesis method on the thermal and sintering properties of copper nanoparticles for use in microscale additive manufacturing processes," *Addit. Manuf.*, vol. 21, pp. 17–29, May 2018, doi: 10.1016/j.addma.2018.02.008.

[8] N. K. Roy *et al.*, "A Comprehensive Study of the Sintering of Copper Nanoparticles Using Femtosecond, Nanosecond, and Continuous Wave Lasers," *J. Micro Nano-Manuf.*, vol. 6, no. 010903, Dec. 2017, doi: 10.1115/1.4038455.

[9] "Neural Network for Nanoscience Scanning Electron Microscope Image Recognition | Scientific Reports." Available: https://www.nature.com/articles/s41598-017-13565-z

[10] M. Ziatdinov *et al.*, "Deep Learning of Atomically Resolved Scanning Transmission Electron Microscopy Images: Chemical Identification and Tracking Local Transformations," *ACS Nano*, vol. 11, no. 12, pp. 12742–12752, Dec. 2017, doi: 10.1021/acsnano.7b07504.

[11] "A Deep Learning Approach to Identify Local Structures in Atomic-Resolution Transmission Electron Microscopy Images - Madsen - 2018 - Advanced Theory and Simulations - Wiley Online Library." Available: https://onlinelibrary.wiley.com/doi/full/10.1002/adts.201800037

[12] "Resolution enhancement in scanning electron microscopy using deep learning | Scientific Reports." Available: https://www.nature.com/articles/s41598-019-48444-2

[13] F. Pellegrino *et al.*, “Machine learning approach for elucidating and predicting the role of synthesis parameters on the shape and size of TiO2 nanoparticles,” *Sci. Rep.*, vol. 10, no. 1, p. 18910, Nov. 2020, doi: 10.1038/s41598-020-75967-w.
[14] B. Lee *et al.*, “Statistical Characterization of the Morphologies of Nanoparticles through Machine Learning Based Electron Microscopy Image Analysis,” *ACS Nano*, vol. 14, no. 12, pp. 17125–17133, Dec. 2020, doi: 10.1021/acsnano.0c06809.
[15] P. Monchot *et al.*, “Deep Learning Based Instance Segmentation of Titanium Dioxide Particles in the Form of Agglomerates in Scanning Electron Microscopy,” *Nanomaterials*, vol. 11, no. 4, Art. no. 4, Apr. 2021, doi: 10.3390/nano11040968.
[16] “Multi defect detection and analysis of electron microscopy images with deep learning - ScienceDirect.” Available: https://www.sciencedirect.com/science/article/pii/S0927025621003037
[17] “Robust autofocusing for scanning electron microscopy based on a dual deep learning network | Scientific Reports.” Available: https://www.nature.com/articles/s41598-021-00412-5
[18] G. Dahy, M. M. Soliman, H. Alshater, A. Slowik, and A. Ella Hassanien, “Optimized deep networks for the classification of nanoparticles in scanning electron microscopy imaging,” *Comput. Mater. Sci.*, vol. 223, p. 112135, Apr. 2023, doi: 10.1016/j.commatsci.2023.112135.
[19] O. G. Dibua, A. Yuksel, N. K. Roy, C. S. Foong, and M. Cullinan, “Nanoparticle Sintering Model: Simulation and Calibration Against Experimental Data,” *J. Micro Nano-Manuf.*, vol. 6, no. 041004, Nov. 2018, doi: 10.1115/1.4041668.
[20] O. G. Dibua *et al.*, “A Study of the Electrical Resistivity of Sintered Copper Nanoparticles,” 2022, Available: https://hdl.handle.net/2152/117279